HAL
open science

Statistical steady state in turbulent droplet condensation

Christoph Siewert, Giorgio Krstulovic, Jérémie Bec

To cite this version:

Christoph Siewert, Giorgio Krstulovic, Jérémie Bec. Statistical steady state in turbulent droplet condensation. Journal of Fluid Mechanics, 2017, 810, pp.254-280. 10.1017/jfm.2016.712 . hal-02363029

HAL Id: hal-02363029

https://hal.science/hal-02363029v1

Submitted on 17 Jan 2024

HAL is a multi-disciplinary open access archive for the deposit and dissemination of scientific research documents, whether they are published or not. The documents may come from teaching and research institutions in France or abroad, or from public or private research centers.

L'archive ouverte pluridisciplinaire **HAL**, est destinée au dépôt et à la diffusion de documents scientifiques de niveau recherche, publiés ou non, émanant des établissements d'enseignement et de recherche français ou étrangers, des laboratoires publics ou privés.

arXiv:1603.04704v2 [physics.flu-dyn] 5 Dec 2016

Statistical steady state in turbulent droplet condensation

Christoph Siewert, Jérémie Bec, and Giorgio Krstulovic

Université Côte d'Azur, Observatoire de la Côte d'Azur, CNRS, Laboratoire Lagrange, 06300 Nice, France.

(Received xx; revised xx; accepted xx)

Motivated by systems in which droplets grow and shrink in a turbulence-driven supersaturation field, we investigate the problem of turbulent condensation in a general manner. Using direct numerical simulations we show that the turbulent fluctuations of the supersaturation field offer different conditions for the growth of droplets which evolve in time due to turbulent transport and mixing. Based on that, we propose a Lagrangian stochastic model for condensation and evaporation of small droplets in turbulent flows. It consists of a set of stochastic integro-differential equations for the joint evolution of the squared radius and the supersaturation along the droplet trajectories. The model has two parameters fixed by the total amount of water and the thermodynamic properties, as well as the Lagrangian integral timescale of the turbulent supersaturation. The model reproduces very well the droplet size distributions obtained from direct numerical simulations and their time evolution. A noticeable result is that, after a stage where the squared radius simply diffuses, the system converges exponentially fast to a statistical steady state independent of the initial conditions. The main mechanism involved in this convergence is a loss of memory induced by a significant number of droplets undergoing a complete evaporation before growing again. The statistical steady state is characterised by an exponential tail in the droplet mass distribution. These results reconcile those of earlier numerical studies, once these various regimes are considered.

1. Introduction

There are many systems where it is necessary to quantify the rate at which droplets shrink and grow in a turbulent environment. The efficiency and environmental impact of a number of propulsion or energy production systems (diesel engine, gasoline engines with direct injection, cryogenic rocket engines, steam turbines, fuel cell ...) depend on the control of evaporation or condensation processes. In natural contexts the prime example is the radiative transfer due to clouds on Earth (Grabowski & Wang 2013) and other planets (Ingersoll *et al.* 2004), which strongly depends upon the microphysics of the droplet growth. In both engineered and natural situations turbulence can have a strong influence (see for example Reveillon & Demoulin 2007; Devenish *et al.* 2012). Due to the variety of such systems we want to reevaluate the problem of turbulent condensational growth in a general manner and ask, from a fluid dynamicist viewpoint, what are the effects of supersaturation fluctuations and of the turbulent transport of droplets on the evolution of the droplet size distribution. Therefore, we want to find a simplified description of the general problem, which still covers the main physical process, identify the main parameters and study the basic behavior of the system as a function of these parameters.

Most work on droplet condensation in turbulence is motivated and applied to terrestrial clouds. An open question is whether turbulent effects can bridge the droplet size gap

in which neither the classical growth by diffusion, nor the classic collision-coalescence growth are efficient (Shaw 2003; Devenish *et al.* 2012; Grabowski & Wang 2013). A condensational broadening of the droplet size distribution by turbulent transport and mixing would increase the collision likelihood. However, using mean-field arguments Bartlett & Jonas (1972) came to the conclusion that the droplet size distribution stays narrow also when turbulent updrafts are taken into account. Such mean-field arguments have anyhow two drawbacks: Firstly, as noticed by Srivastava (1989), the local supersaturation in the direct vicinity of a droplet can differ from one droplet to another and from the average supersaturation. These differences in local supersaturation can be due to variations in the amount of vapor consumption by droplets with different sizes as well as fluctuations due to turbulence. Indeed, it was found using stochastic modeling (Kulmala *et al.* 1997; Khvorostyanov & Curry 1999; McGraw & Liu 2006) that, due to such fluctuations, droplets can exists even if the global supersaturation is negative. Hence, in such models the droplet size spectra are broader than those obtained by mean-field models.

The second drawback of mean-field models is the assumption that the tracked volume does not mix during the evolution. However, it is well known that this is generally not true in turbulent flows. For example, inertialess droplets (tracers) separate explosively following Richardson diffusion, leading to a strong mixing. Based on this picture Lasher-Trapp *et al.* (2005) and Sidin *et al.* (2009) used large-eddy simulations and kinematic simulations in which they backtrace all droplets that are in a specific volume at a final time. As they come from very different locations, a broad droplet size distribution is observed in the final volume. However, such a two-step approach is not well suited to account for the mutual influence and competition between droplets that were close to each other in the past.

One way to overcome these issues is to perform direct numerical simulations (DNS) for the joint evolutions of the fluid velocity, temperature, and water vapor, without introducing any ad-hoc modelling. This approach naturally accounts for the above-mentioned points, the spatial and temporal fluctuations in the supersaturation and the turbulent transport and mixing. However, such simulations are computationally very demanding and became thus feasible only rather recently. Vaillancourt *et al.* (2002) were the first to perform DNS of the turbulent fields coupled with a Lagrangian droplet model. They find only a very little increase in the broadening of the droplet size spectra, compared to simulations without turbulence (Vaillancourt *et al.* 2001) and explain this by the decorrelating effect of turbulence between the droplet size and the supersaturation in its vicinity.

Celani *et al.* (2005) have performed two-dimensional DNS in order to increase the domain size and the range of turbulent eddies. They find the opposite trend, namely a very broad droplet size spectrum, but which might originate from neglecting the influence of the droplets on the supersaturation field. Later they contrast their results incorporating more realistic physical treatments. In Celani *et al.* (2008), they implement a detailed droplet activation scheme and obtain that the droplet size spectra are still very broad, independently of the activation process. In Celani *et al.* (2007) and Celani *et al.* (2009), they account for the back reaction of droplets on the supersaturation field and observe a negative mean supersaturation and a reduction of the spectral broadening that eventually becomes stationary. Nevertheless, the spectra they measure are still very broad.

Paoli & Shariff (2009) have performed three-dimensional DNS of turbulent condensation with a large-scale forcing acting not only on the fluid velocity but also on the temperature and vapor fields. However, they do not specifically focus on estimating spectral broadening but rather on developing a stochastic model intended to be used

in large-eddy or Reynolds-averaged simulations. Lanotte *et al.* (2009) find in 3D DNS that the droplet surface area has a distribution very close to a Gaussian and that the broadening is rather small, in agreement with the findings of Vaillancourt *et al.* (2002). However this broadening, measured for instance by the standard deviation of the droplet surface area, increases with both time and Reynolds number. By dimensional arguments, they extrapolate this behaviour to the large Reynolds numbers of clouds and predict a significant broadening. Very recently, Sardina *et al.* (2015) repeated the investigations of Lanotte *et al.* (2009) with longer simulation times and higher resolutions. They found that the standard deviation of the droplet surface area increases proportionally to the square root of time. Additionally, they make use of a stochastic model very similar to the one of Paoli & Shariff (2009) to obtain that the constant factor in this behaviour is proportional to the Reynolds number.

Such an approach is particularly promising for designing realistic models for droplet condensation in turbulent flows. However, the various contradicting results of DNS described above still lack a clear understanding. They show either a strong broadening or very few broadening when the results are not extrapolated to high Reynolds numbers. Questions remain on the origins of these differences: Are they due to dissimilarities in settings or governing equations? Does the problem lack of universality and depend on dimensionality, initial conditions, and activation processes?

The present work aims at providing some answers to these questions. The paper is organised as follows: In §2.1 we first describe the governing equations of our simplified system. The variations in temperature and vapor concentration are modeled in terms of a single scalar field, the supersaturation, which is passively advected by the flow. Droplets are passively transported by a homogeneous, isotropic turbulent flow. The droplets can completely evaporate, without disappearing, and grow again if they reach a positive-supersaturation region. Based on dimensional analysis (§2.2), the turbulent phase change is described by two relevant timescales: the droplet growth rate and the response time of the supersaturation field upon condensation or evaporation. Depending on whether these characteristic times are greater or smaller than turbulent timescales and the observation time, one expects different regimes. We confirm the existence of these regimes by three-dimensional direct numerical simulations (§2.3). We then introduce in §3.1 a stochastic integro-differential Lagrangian model, which imposes the global mass conservation of liquid and vapor and is expected to be valid for timescales much larger than the Lagrangian correlation time. In §3.2 this model is shown to reproduce well the results of DNS. In addition we find that the condensation process converges to a statistically steady state, so that the droplet size distribution and the fluctuations of the supersaturation field become independent of time and initial conditions. For both the model and the DNS, the stationary probability distribution function (PDF) of droplet masses is shown to have an exponential tail (§4.1 and §4.2) that we characterise in §4.3 as a function of the relevant parameters. We show that after a Brownian stage during which the droplet surface area just diffuses (§5.1), the exponential convergence to the steady state occurs once a significant fraction of droplets has completely evaporated at least once (§5.2). Finally, we draw concluding remarks in §6. A list of symbols can be found in Appendix A.

2. General Framework

To concentrate on the influence of turbulence we choose idealized conditions. This enables us to make analytical predictions but, of course, at the risk of missing important physical phenomena that might be important for applications. That is why we state

precisely in the following under which conditions the equations are valid. The equations are stated in a general form in §2.1, the numerical treatment will be described in §2.3.

2.1. *Governing Equations*

The immediate neighborhood of a given droplet is characterized by a local value of the supersaturation field $s = p/p_s - 1$ (where p is the vapour partial pressure and p_s the saturation pressure), which induces the growth of its squared radius r^2, i.e. the droplet surface area:

$$\frac{dr^2}{dt} = \begin{cases} 2a_3 s & r^2 \geqslant 0, \\ 0 & r^2 = 0 \;\&\; s < 0. \end{cases} \tag{2.1}$$

The coefficient a_3 is assumed constant, *i.e.* the small temperature dependence is neglected. It is here understood that the timescale associated with the establishment of vapour diffusion is faster than the external timescales especially the smallest scales of turbulence, the Kolmogorov scale η (see, *e.g.*, Pruppacher & Klett 1997; Vaillancourt *et al.* 2001, for a detailed derivation). This approximation might become invalid in some highly turbulent environments encountered in technical applications where η can be very small. Additionally, it is assumed that the droplet volume loading is small enough to ensure no overlap between the diffusion regions of different droplets. Finally, curvature and salinity effects relevant for the activation and affecting the growth of very small droplets are neglected (Celani *et al.* 2008). Instead, we assume that a completely evaporated droplet is simply reactivated if it is located in a region with positive supersaturation playing the role of a condensation nuclei that stays in the system. We show in §4 that the specific type of boundary condition imposed at $r = 0$ is not important for the large-value tail of the droplet size distribution, *i.e.* faraway from the zero-size boundary.

The growing and shrinking droplets are transported by a turbulent gas velocity $\mathbf{u}$ according to the Stokes drag law

$$\frac{d\mathbf{v}}{dt} = -\frac{1}{\tau_d(r)}\left[\mathbf{v} - \mathbf{u}(\mathbf{x}, t)\right], \tag{2.2}$$

where $\mathbf{x}$ and $\mathbf{v}$ are the particle position and velocity, $\tau_d = 2\rho_d r^2/(9\rho\nu)$ is the droplet response time, ρ_d its mass density, and ρ and ν are the gas mass density and kinematic viscosity, respectively. The Stokes drag approximation is valid for very small and heavy liquid droplets. The droplet radius r has to be smaller than the smallest scale of turbulence, the Kolmogorov dissipative scale $\eta = \nu^{3/4}/\varepsilon^{1/4}$, where ε is the mean kinetic energy dissipation rate of the turbulent gasflow. Although the liquid to gas density ratio ρ_d/ρ is typically large, the droplet size and therewith its mass are typically small enough for gravitational acceleration to be neglected. A posteriori we know that in our parameter range the droplet motion is practically identical to tracer motion as the droplet response time stays negligibly small. Furthermore, for the smallest droplets Brownian motion might become important.

The gas velocity $\mathbf{u}$ evolves according to the incompressible Navier-Stokes equation

$$\frac{\partial \mathbf{u}}{\partial t} + \mathbf{u}\cdot\nabla\mathbf{u} = -\frac{1}{\rho}\nabla p + \nu\nabla^2\mathbf{u} + \phi_u\,, \quad \nabla\cdot\mathbf{u} = 0\,, \tag{2.3}$$

where p is the pressure and ϕ_u is a large-scale forcing, which maintains turbulence in a developed regime. Mixing with the environment at the boundaries, often called entrainment and detrainment, is neglected. Additionally, as for the droplets, we neglect temperature and gravity effects, including buoyancy. This might be the strongest approximation as latent heat release upon condensation is often a strong source for natural moist

convection. However, without the anisotropies introduced by buoyancy and edge effects, we generate a homogeneous and isotropic turbulent flow. This drastically simplifies the statistics and their interpretation and thus motivated us to use these approximations as a first step. As a matter of fact, we will show that some of our results are similar to those of Celani *et al.* (2007) who accounted for the temperature field and buoyancy effects.

Since thermal effects are neglected, it is not necessary to treat the temperature and vapour fields separately. Instead the supersaturation s can be modeled as passive scalar coupled to the Lagrangian particles

$$\frac{\partial s}{\partial t} + \mathbf{u} \cdot \nabla s = \kappa \nabla^2 s - \sum_{i=1}^{N} 4\pi \rho_d a_2 a_3 r_i \, s(\mathbf{x}_i, t) \, \delta(\mathbf{x}_i - \mathbf{x}) + \phi_s \,, \tag{2.4}$$

where κ is the molecular diffusivity of the vapour inside the gas. The second term on the right-hand side accounts for the local change in supersaturation due to the presence of N droplets. There, $\mathbf{x}_i$ denotes the position of the ith droplet and the coefficient a_2 accounts for both the change in vapour mass and temperature due to the condensation or evaporation. We assume again that the temperature dependence of a_2 is negligible. There are two common choices for the forcing term ϕ_s. The first one, often used in experiments on passive scalars, is to impose a mean gradient (Warhaft 2000). In atmospheric conditions there is often a vertical temperature gradient, so that updrafts increase the supersaturation (Squires 1952; Twomey 1959). Hence, the DNS studies in the context of cloud physics (see §1) considered $\phi_s = \mathbf{u} \cdot (0, 0, a_1)$, where a_1 is a constant that depends weakly on temperature. If a_1 is assumed to be constant, this forcing is just a special form of the mean gradient forcing. The second choice, more commonly used in the physics community and in numerical simulations on the advection of passive scalars by a turbulent flow, is to force also the supersaturation field by a large-scale forcing. The properties of the supersaturation field without droplets, which is then a passive scalar, are thus well known. Even if this has been recently questioned by Gotoh & Watanabe (2015), one expects such properties to not depend on the specific form of forcing and to display some universality. For instance, coherent structures are present at all length scales, separated by regions where the field undergoes significant fluctuations, the so-called fronts associated with very sharp gradients (Celani *et al.* 2001). If there is no mean forcing input ($\int_v \phi_s d^3x = 0$), the mean value of supersaturation remains constant. Then, the system (2.1)-(2.4) conserves the global mass of liquid and vapour

$$wv = \int_v (s(x,t) + 1) \, \mathrm{d}^3x + a_2 \sum_{i=1}^{N} \rho_d \frac{4}{3} \pi \, r_i(t)^3 = \text{const} \,. \tag{2.5}$$

Similar mass balances have been proven to be useful to obtain analytical results (Pinsky *et al.* 2013; Devenish *et al.* 2016). Motivated by our idea to concentrate on the influence of turbulent mixing, we choose here to use a large-scale forcing for ϕ_s. We will show in §6 that we can explain the results of those DNS studies with updraft forcing by the outcomes of our simulations. However, in contrast to assuming a mean gradient, our choice ensures the statistical homogeneity and isotropy of the scalar field s, and hence of the droplet sizes.

2.2. *Qualitative Predictions*

In the various systems (see §1) the physical parameters such as the kinematic viscosity of the gas, the number of droplets and the total amount of liquid and vapour can take very different values. To treat the problem of turbulent condensation as generally as

possible, *i.e.* independently of any specific application, we analyse here dimensionless equations. Thereby, non-dimensional groups are obtained by dimensional analysis that are determining the solutions of the system of differential equations. As long as the assumptions made in the previous subsection are not violated, the solutions we obtain can be applied to a specific application, once rescaling them together with time and lengthscales using the specific dimensional parameters. Non-dimensional quantities are always written in capital letters to distinguish them from the dimensional quantities written in lowercase.

The turbulent fluctuations of supersaturation along droplet trajectories are essentially correlated over the large scales, because to leading order, droplets are Lagrangian objects. We thus decide to use as a reference length, the large scale $l_0 = u_{\rm rms}^3/\varepsilon$, where $u_{\rm rms}$ is the root-mean-square velocity, and as a reference time the large eddy turnover time $t_0 = l_0/u_{\rm rms}$.

Applying this to the Navier-Stokes equations (2.3) leads to the Reynolds number

$$Re = \frac{\tau_\nu}{t_0} = \frac{l_0^2/\nu}{t_0}\,, \tag{2.6}$$

which is the ratio of viscous mixing time scale to the turbulent advection time scale. In principle we want the Reynolds number as large as possible in order to have a large separation between the forcing and the dissipation scales. However, the computational effort increases with the resolution, such that most of our simulations will be conducted at $Re = 2100$.

The droplet equation of motion (2.2) leads to introduce the large-scale Stokes number

$$St = \frac{\tau_d}{t_0} = \frac{2\rho_d \bar{r}^2}{9\rho\nu t_0}. \tag{2.7}$$

A priori the droplet sizes evolve with time, and so do the Stokes numbers. Motivated by the global mass balance eq. (2.5) we choose here and in the following to use the droplet mass averaged over the whole population as typical size $\bar{r} = f(t)$, namely $\bar{r} = \langle r(t)^3\rangle^{1/3}$. As the droplets are typically small, we expect the Stokes number to be small, so that inertia effects, such as clustering, are weak even on the smallest scales.

The supersaturation equation (2.4) provides two timescale ratios: The Schmidt number

$$Sc = \frac{\tau_\kappa}{\tau_\nu} = \frac{l_0^2/\kappa}{l_0^2/\nu}, \tag{2.8}$$

that we only consider to be one and the timescale of change in supersaturation due to condensation

$$\frac{\tau_s}{t_0} = \frac{1}{4\pi\rho_d a_2 a_3 n_d \bar{r} t_0}, \tag{2.9}$$

which is obtained from a spatial average and depends on both the characteristic radius $\bar{r}$ and the droplet number density n_d.

The supersaturation diffusion-advection equation (2.4) is linear and hence the proper choice for the reference value of s is not straightforward. We select its standard deviation $s_{\rm rms}$ in the absence of droplets. From the droplet growth equation (2.1) a time scale arises, which we call hereafter the condensation timescale

$$\frac{\tau_c}{t_0} = \frac{\bar{r}^2}{2a_3 s_{\rm rms} t_0}. \tag{2.10}$$

This condensation timescale did not receive much attention in recent DNS studies of homogeneous condensation (Vaillancourt *et al.* 2002; Celani *et al.* 2005; Lanotte *et al.*

2009; Sardina *et al.* 2015). However it is known and used in the context of mixing of sub- and supersaturated regions. Based on the notation in reacting flows a Damköhler number is constructed to compare the turbulent mixing timescale to the time for phase change (Devenish *et al.* 2012). In this sense, the dimensionless quantities defined in Eqs. (2.9) and (2.10) can be seen as inverse Damköhler numbers. This raises the question about the relevant timescales that characterise the system. From their DNS results, Kumar *et al.* (2012) concluded that the Damköhler number based on the supersaturation timescale is the relevant one. However, Lehmann *et al.* (2009) argued that the timescale of the coupled system might be very different from both the condensation and supersaturation timescales.

We give here some preliminary heuristic arguments on possible asymptotic behaviour of the system. Let us consider the supersaturation equation (2.4): If τ_s is very large, the influence of the particle on the supersaturation field is small, *i.e.* its evolution is dominated by turbulent mixing characterised by the timescale t_0. Conversely, if this supersaturation timescale is very small, the condensation or evaporation of droplets dominates the variations of s and the characteristic timescale for the supersaturation evolution is τ_s. The supersaturation field thus changes on a timescale given by the minimum of t_0 and τ_s. Assume now that the condensation timescale τ_c is much larger than the minimum of t_0 and τ_s, meaning that the droplet sizes change slowly compared to the supersaturation field. This was implicitly assumed in mean-field models and corresponds to the homogeneous case (small Damköhler number) in the context of chemical reactions. In this case individual droplets experience a fast changing supersaturation, which to leading order can be approximated as a random white noise. From Eq. (2.1), one infers that their surface area r^2 follows a Brownian motion. This implies that the standard deviation of the droplets surface σ_{r^2}, which gives a measure of the spectral broadening, evolves as $\propto \sqrt{t}$. Conversely, if we now consider that τ_c is much smaller than the minimum of t_0 and τ_s, the droplet sizes change faster than the supersaturation value along their trajectories. We are then in the inhomogeneous limit, where more complex dynamics can be expected. Droplets experience a quasi constant supersaturation value for a long time and change their sizes rapidly. This could lead to both very large droplets and complete evaporation. We thus expect in this case a very broad droplet size spectrum.

2.3. *Direct Numerical Simulations*

We conduct a series of direct numerical simulations of the flow and the supersaturation field with the pseudo-spectral code LaTu (Homann *et al.* 2007) in a cubic, periodic domain. The gas flow forcing ϕ_u is chosen to keep constant the energy content of the first two shells of wavenumbers in Fourier space. The supersaturation forcing ϕ_s is Gaussian, white-noise in time and concentrated at wavenumbers with moduli between 1 and 2.5. The various non-dimensional parameters are reported in Table 1. Most simulations are performed at a resolution of 512^3 collocation points, corresponding to a Taylor micro-scale Reynolds number $R_\lambda \approx 180$. The ratio between the largest and the smallest time scales is $t_0/\tau_\eta \approx 50$, indicating a sufficient scale separation. Additionally, selected simulations are repeated at decreased (256^3) and increased (1024^3) resolutions, corresponding to $R_\lambda \approx 100$ and $R_\lambda \approx 320$, respectively, in order to test possible Reynolds number dependence. We only consider cases where the Schmidt number is unity and the Eulerian mean supersaturation is initially zero. The fields are evolved until a statistical steady state is reached. Then ten millions equal-sized droplets are randomly released in the domain with a large-scale Stokes number of $St = 2.3 \times 10^{-5}$ to ensure that particle inertia is initially negligible. These Lagrangian droplets, together with their sizes, are subsequently integrated according to Eqs. (2.1) and (2.2) using a tri-cubic interpolation

N_x^3	$\frac{\nu}{l_*^2/t_*}$	$\frac{\eta}{l_*}$	$\frac{\tau_\eta}{t_*}$	$\frac{u_{\rm rms}}{l_*/t_*}$	$\frac{l}{l_*}$	$\frac{t_0}{t_*}$	$\frac{t_u}{t_*}$	$\frac{t_s}{t_*}$	Re	R_λ
256^3	$3.1\,10^{-3}$	$1.32\,10^{-2}$	$5.7\,10^{-2}$	1.20	1.83	1.53	0.31	0.72	715	100
512^3	$4.6\,10^{-4}$	$3.1\,10^{-3}$	$2.2\,10^{-2}$	1.0	1.0	1.0	0.36	0.64	2175	180
1024^3	$1.53\,10^{-4}$	$1.4\,10^{-3}$	$1.2\,10^{-2}$	1.04	1.03	1.02	0.32	0.60	6800	320

TABLE 1. Parameters of the numerical simulations for the turbulent gasflow with respect to the large-scale values of the intermediate resolution case denoted as l_* and t_*: N_x^3 number of spatial collocation points; ν kinematic viscosity; $\eta = \nu^{3/4}/\varepsilon^{1/4}$ Kolmogorov dissipative scale; $\tau_\eta = \nu^{1/2}/\varepsilon^{1/2}$ Kolmogorov time; $u_{\rm rms}$ root-mean square velocity; $l_0 = u_{\rm rms}^3/\varepsilon$ large scale; $t_0 = u_{\rm rms}^2/\varepsilon$ large-eddy turnover time; t_u integral timescale of the Lagrangian velocity autocorrelation; t_s integral timescale of the Lagrangian scalar autocorrelation; $Re = u_{rms} l_0/\nu$ large-scale Reynolds number; $R_\lambda = \sqrt{15}\, u_{\rm rms}^2 \tau_\eta^2/\eta^2$ Taylor microscale Reynolds number.

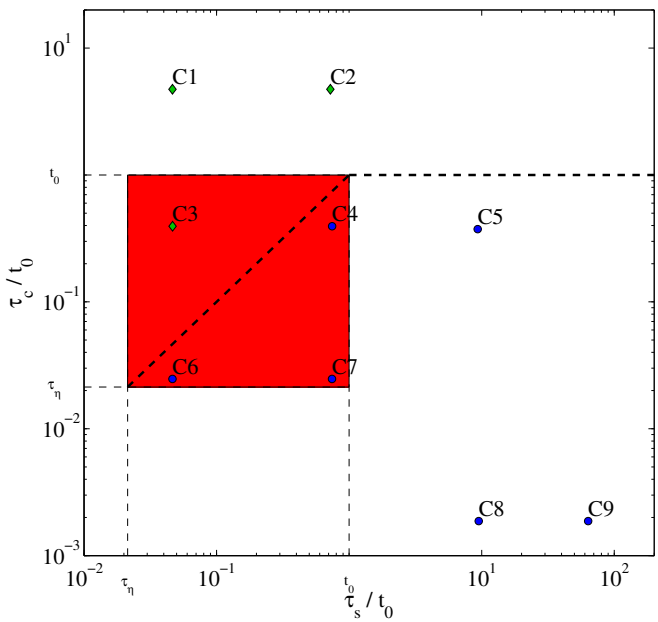

FIGURE 1. Plot showing the parameter space explored by DNS as labeled points in terms of the condensation timescale τ_c and the supersaturation timescale τ_s. The red area spans from the Kolmogorov time scale τ_η to the large-eddy turnover time t_0 to indicate the turbulent inertial range. The thick dashed line separates the region above in which $\tau_c > \min(\tau_s, t_0)$ with green diamonds from the region with $\tau_c < \min(\tau_s, t_0)$ with blue circles.

of the gas velocity and of the supersaturation value at the particle position. The back-reaction of the droplets onto the supersaturation field in Eq. (2.4) is performed by linear extrapolation to the nearest collocation points.

The parameter space explored in terms of the condensation and supersaturation time scales τ_c and τ_s is visualised in Fig. 1 and additionally summarized in Table 2. Different combinations are chosen in or close to the turbulent inertial range in order to detect possible interferences or resonances between the various physical processes.

In §2.2 we anticipated two different asymptotic regimes. For a first impression of these

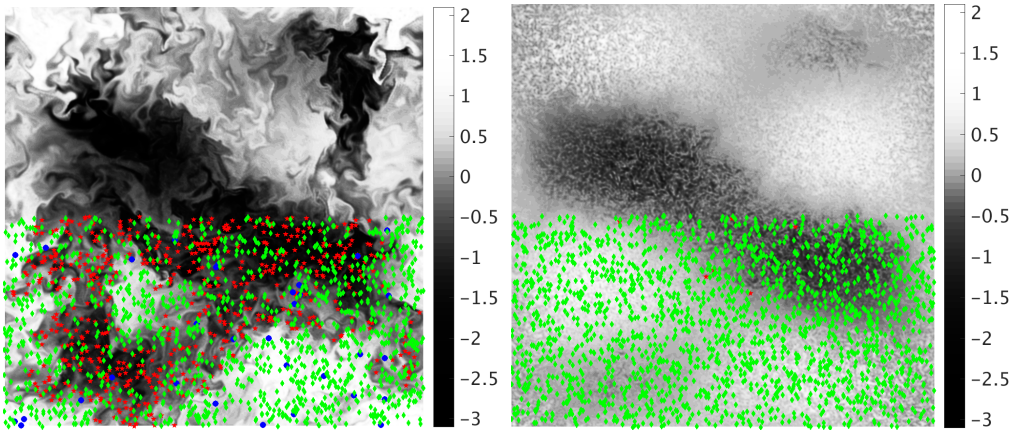

FIGURE 2. Slice of thickness 0.4 η through the 3D supersaturation field at $t = 3.1\ t_0$; Left: Case $C4$; Right: Case $C3$. The value of s/s_{rms} are given as grayscale contour plot. Additionally the droplets are superpositioned in the lower half. Their size is increased for better visibility, their color indicates their real size: Red stars are for $r^2 = 0$, green diamonds for the intermediate sizes ($0 < r^2 < 2\langle r^2 \rangle$), and blue circles for $r^2 > 2\langle r^2 \rangle$.

	C1	C2	C3	C4	C5	C6	C7	C8	C9
τ_c/t_0	4.737	4.737	0.3948	0.3948	0.3740	0.02467	0.02467	0.001870	0.001870
τ_s/t_0	0.04649	0.7213	0.04654	0.7436	9.3253	0.04648	0.7427	9.491	63.509

TABLE 2. The parameter space explored by the DNS cases C1 to C9 in terms of the condensation and supersaturation time scales τ_c and τ_s.

two regimes we select the cases $C3$ and $C4$ for visualisation. They feature the same value of the condensation timescale $\tau_c < t_0$, but $C4$ has a larger value of the supersaturation timescale $\tau_s < t_0$, such that we expect to obtain for these instances the two different asymptotic regimes. Two-dimensional cuts of the two supersaturation fields are shown in Fig. 2. The left-hand panel shows the case $C4$ where $\tau_c < \tau_s < t_0$. The supersaturation field clearly looks like a turbulent passive scalar as described in §2.1 (see Warhaft 2000, for a review). Hence, the influence of the droplets is practically unnoticeable, except globally as the spatial average of s is negative. In the right-hand panel of Fig. 2 the case $C3$, where $\tau_s < \tau_c < t_0$, is represented and displays a completely different behaviour. The local fluctuations of s are strongly reduced at both positive and negative values. Large-scale structures still exist, but intermediate-scale variations are smoothed out by the droplet-vapour exchange. At fine scales the influence of the individual droplets can be recognized. Their positions are superimposed on the lower half of Fig. 2. There are very few completely evaporated droplets, but no droplet that has doubled its surface area after 3.1 t_0. For comparison, in the case $C4$ (left-hand panel of Fig. 2), there are large droplets and a huge portion of evaporated droplets can be found in regions with a negative supersaturation.

3. Stochastic Model

To understand further the different regimes discussed in §2.2, we develop here a stochastic model which is giving a simple approximation for the global system (2.1)-(2.4). This model is supposed to give predictions for the global evolution of the size distribution, rather than a good approximation for the time evolution of single droplets. In that sense, this model should be intended as a PDF model, rather than a pure Lagrangian approximation. It is expected to reproduce well the one-point one-time joint statistics of r and s but, in principle, cannot be used for multiple-point or multiple-time statistics.

3.1. *Derivation*

We are interested in the behaviour of the joint distribution of r^2 and s along droplet trajectories at large times. The large-scale Stokes number being small, we thus assume that droplet inertia can be neglected. Following ideas borrowed from PDF modelling of turbulent mixing (see Pope 2000), we assume that along droplet trajectories, the variations of supersaturation due to diffusion and forcing can be approximated at large times by a Langevin (Ornstein–Uhlenbeck) process. The correlation time should then be the integral time scale of the Lagrangian scalar autocorrelation t_s and the drift the (time-dependent) Eulerian average of the supersaturation field $\langle s\rangle_E$. When taking into account the variation of supersaturation due to condensation or evaporation of the droplet from Eq. (2.4), this leads to model the evolution of s along droplets as

$$\frac{\mathrm{d}s}{\mathrm{d}t} = -\frac{1}{t_s}(s - \langle s\rangle_E) - \frac{1}{\tau_s}\frac{r}{\bar{r}}\,s + \sqrt{\frac{2s_{\mathrm{rms}}^2}{t_s}}\,\xi(t), \tag{3.1}$$

where ξ is the standard white noise. Hence, note that this evolution equation is a stochastic differential equation, which has to be taken into account when, e.g., computing the moments of s. The evolution equation is of course supplemented by Eq. (2.1) to account for the time variations of the droplet radius r. This modelling involves the Eulerian average $\langle s\rangle_E$ of the supersaturation field which is not directly given by a Lagrangian approach but can be inferred from the global mass conservation of liquid and vapour. We indeed have from (2.5) combined with (2.9) and (2.10)

$$w = \langle s\rangle_E + 1 + \frac{2}{3}\frac{\tau_c}{\tau_s}s_{\mathrm{rms}} = \mathrm{const}, \quad \text{so that } \langle s\rangle_E = (w-1) - \frac{2}{3}\frac{\tau_c}{\tau_s}s_{\mathrm{rms}} \propto -\langle r^3\rangle. \tag{3.2}$$

The Eulerian averaged supersaturation is thus a global quantity that depends on the full distribution of r. In that sense the system is not closed at the level of a single droplet and the associated Fokker–Planck equation is an integro-differential equation. Because of this, our model differs from that proposed by Paoli & Shariff (2009). They have indeed used the Lagrangian mean of s instead of the Eulerian one. Additionally, we want to emphasize that the supersaturation along trajectories is correlated over times corresponding to the Lagrangian integral timescale of the scalar t_s. Table 1 shows in agreement with Yeung (2001) that t_s generally differs from the large eddy turnover time t_0 used by Paoli & Shariff (2009) and the Lagrangian integral timescale of the velocity t_u used by Sardina *et al.* (2015).

To single out the relevant parameters, we next rescale time t by t_s, the supersaturation s by s_{rms}, and the droplet radius r by $\bar{r}\sqrt{t_s/\tau_c} = \sqrt{2a_3 s_{\mathrm{rms}} t_s}$. The model then reads

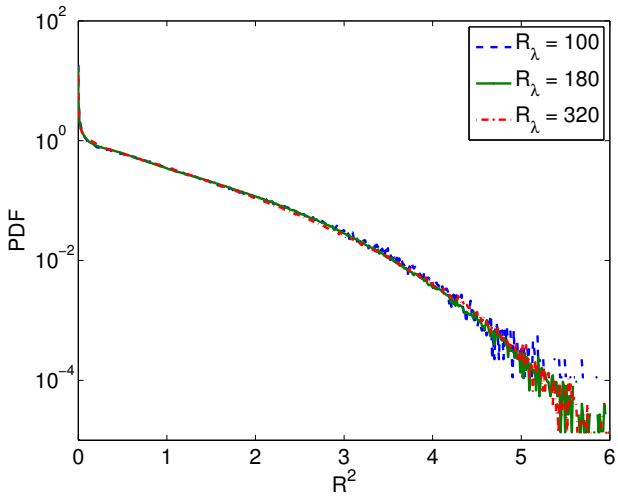

FIGURE 3. Comparison of three DNS runs with increasing resolutions and therewith Taylor scale-based Reynolds numbers but same parameters τ_c/t_s and τ_s/t_s, namely that of case $C8$, by the means of the PDF of R^2 at $t = 6.2\ t_s$: Blue 256^3 at $R_\lambda = 100$; Green 512^3 at $R_\lambda = 180$; Red 1024^3 at $R_\lambda = 320$.

$$\frac{dR^2}{dT} = \begin{cases} S & R^2 \geqslant 0 \\ 0 & R^2 = 0 \ \& \ S < 0 \end{cases} \tag{3.3a}$$

$$\frac{dS}{dT} = \left(\langle W \rangle - \frac{2}{3} A \langle R^3 \rangle \right) - S + \sqrt{2}\xi - ARS. \tag{3.3b}$$

The evolution depends upon two parameters: The global mass

$$\langle W \rangle = \frac{w-1}{s_{\mathrm{rms}}} = \langle S \rangle_E + \frac{2}{3} A \langle R^3 \rangle, \tag{3.4}$$

and the constant A, which determines how strongly the evolution of R couples back to the evolution of S. It is given by the two timescales τ_c and τ_s, namely

$$A = \frac{t_s}{\tau_s} \sqrt{\frac{t_s}{\tau_c}} = \sqrt{32 s_{\mathrm{rms}}} \pi \rho_d A_2 A_3^{3/2} n_d t_s^{3/2}. \tag{3.5}$$

To provide evidence that t_s is the correct correlation time, we conduct DNS at various resolutions, *i.e.* varying the Reynolds numbers, while at the same time we keep the dimensionless parameters τ_c/t_s and τ_s/t_s constant. As depicted in Table 1, these parameters would differ by 20 or 25 percent in this Reynolds number range if t_0 or t_u had been used instead. Figure 3 shows the probability density function (PDF) of the normalized droplet surface area R^2 for the three different Reynolds numbers at a specific time T. The collapse of the distribution confirms the role of large-scale mixing and emphasizes the choice of t_s as a reference timescale. As η decreases with the Reynolds number at fixed l_0, we also decreased r accordingly to stay in the Stokes drag limit (see § 2.1). We kept the particle volume loading n_d constant, hence, the number of particles increases with Reynolds number. That is why the R^2 tail contains less statistical noise at higher Reynolds number. Still, by normalizing with the Reynolds number dependent values of t_s and s_{rms} the PDF of $R^2\,(T)$ is collapsing, i.e. if there is any Reynolds number dependence at all it is only very weak.

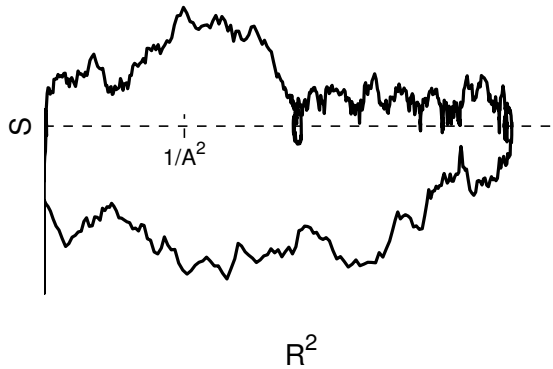

FIGURE 4. Exemplary dynamics in the $R^2 - S$ phase space.

The nonlinear integro-differential stochastic system (3.3) is much simpler than the original governing system of partial-differential equations, but still too complex to be solved analytically. As done by Paoli & Shariff (2009) the evolution of the moments can be written down from the model equations 3.3:

$$\frac{d\langle R^{x+2}\rangle}{dT} = \frac{x+2}{2}\langle SR^x\rangle \tag{3.6a}$$

$$\frac{d\langle S\rangle}{dT} = \langle S\rangle_E - \langle (1+AR)\,S\rangle \tag{3.6b}$$

$$\frac{d\langle S^2\rangle}{dT} = 2\langle S\rangle_E\langle S\rangle - 2\langle (1+AR)\,S^2\rangle + 2 \tag{3.6c}$$

$$\frac{d\langle SR^2\rangle}{dT} = \langle S\rangle_E\langle R^2\rangle + \langle S^2\rangle - \langle (1+AR)\,SR^2\rangle \quad . \tag{3.6d}$$

This is an unclosed hierarchy of equations and can only be solved if additional closure assumptions are made. However, it is possible to understand qualitatively the system dynamics. A typical trajectory in the phase space is shown in Fig. 4. Due to the noise term the supersaturation tends to do Brownian excursions. For negative values of S the droplet shrinks while for positive values the droplet grows. The drift term prevents runaway excursions to $s = \pm\infty$. Note that the non-linear coupling term $-ARS$ is dominant for large droplets $R^2 \gg 1/A^2$. Thereto the larger the droplet is, the faster a positive S is reduced to zero, so that large droplets can growth only on very short timescales. Conversely, an evaporating droplet is less and less effective in pushing its negative supersaturation back to zero and thus has longer and longer time to shrink. Due to this bias it seems reasonable to assume that a droplet cannot grow infinitely large. In the opposite limit, when a droplet completely evaporates (reaches $R = 0$), the dynamics of S decouples from R and the droplet will start growing only once S becomes positive, reinitializing the full process again. There is thus a loss of memory of the previous growth history. Bounded excursions, together with the recurrent memory losses suggest that, at long time, the system should reach a statistical stationary state independent of its initial condition.

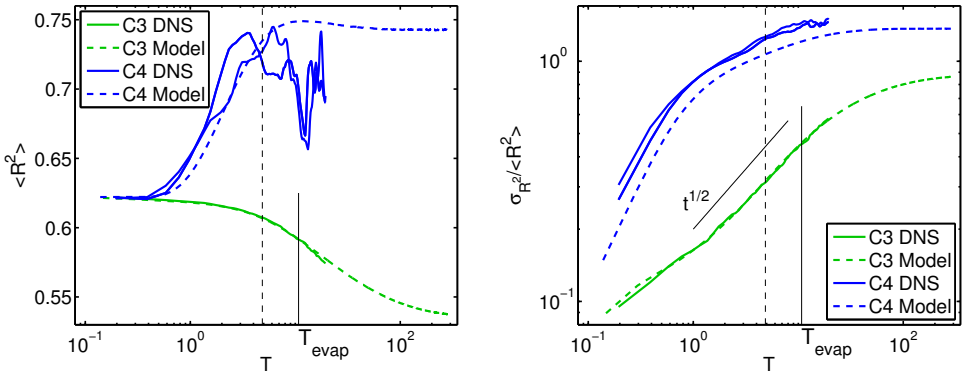

FIGURE 5. Comparison of the DNS (solid lines) with the results of the stochastic model (dashed lines) for the cases $C3$ (green) and $C4$ (blue). Note that for case $C4$ two independent DNS runs are shown. Left: Time evolution of the mean droplet surface area $\langle R^2 \rangle$; Right: Time evolution of the relative standard deviation of the droplet surface area $\sigma_R^2/\langle R^2 \rangle$. The vertical black solid line marks t_{evap} for $C3$ at which $\sigma_R^2/\langle R^2 \rangle$ is predicted to start deviating from the $t^{1/2}$ behavior (see §2.2 for the preliminary heuristic arguments and sec. 5.1 for a detailed derivation of eq. (5.3)). The vertical black dashed line marks the time of the snapshots shown in Fig. 2.

3.2. *Comparison with DNS*

We perform Monte-Carlo (MC) simulations of the system (3.3) for the same parameters as in the DNS cases $C3$ and $C4$ shown in Fig. 2. Thereto the parameters A (3.5) and $\langle W \rangle$ (3.4) are calculated from the DNS initial conditions. Especially t_s and s_{rms} are measured from the initial supersaturation field as the afterwards released droplets change its properties. The parameters A and $\langle W \rangle$ both depend on s_{rms}, hence, the model is sensitive to the value of s_{rms}. The MC simulations allow us to simulate the system for much longer times than for the DNS.

The evolution of $\langle R^2 \rangle$ is shown in the left panel of Fig. 5. In the case $C3$ the mean value of R^2 for both the DNS and the model, first remains relatively constant and then even decreases. In contrast, for the case $C4$, the average of R^2 increases substantially before converging to a constant value. In this case, the model lags a little bit behind the DNS. Additionally, the final value seems to be a few percent higher, although this is not unambiguous as the DNS value strongly fluctuates. That is why we have represented two different realizations of the full DNS C4 in Fig. 5. Given the large amplitude of the variations between these two runs and of the fluctuations as a function of time, the deviations from the model could be explainable by a lack of ensemble averaging. While the number of droplets is the same for the DNS and the MC simulation, the supersaturation in DNS is correlated on the large scales, whereas the random increments are independent in the model. Hence, the number of independent realizations is higher in the model. Ensemble averaging of independent DNS realizations would be needed but is computationally too expensive.

The right panel of Fig. 5 represents the coefficient of variation of the droplet surface area, namely the relative standard deviation $\sigma_R^2/\langle R^2 \rangle$. In the case $C4$ it increases first rapidly and then converges, although more slowly than the mean value, to a value close to one. The model values are slightly lower than the DNS. Nevertheless, for both the model and the DNS, the coefficient of variation is order one, indicating a very broad distribution close to the one given for instance by an exponential distribution. For the case $C3$, the relative standard deviation starts much lower and for a decade of time, the predicted $t^{1/2}$ power-law can be seen in the logarithmic plot. Hence, while the case $C4$ is

already in the steady state in Fig. 2, $C3$ is still in the Brownian motion regime, leading to the very different pictures. However, also in the case $C3$, the model eventually converges to a constant value, *i.e.* a steady state is reached at very large times.

To conclude we want to emphasize two points: First, the MC simulations confirm the above reasoning that, at long times, the system converges to a steady state. Hence, the heuristic arguments of §2.2 actually describe two regimes of the transient system behaviour. Second, the model predictions are representative of the actual dynamics. The simple stochastic model is indeed able to reproduce some results of the DNS surprisingly well. This is unexpected as the turbulence is only modeled trivially and no intermittency or inertia effects are taken into account. The short-time behaviour is perfectly reproduced, while there are deviations for the steady state. However, these deviations are systematic for all DNS runs reported in Fig. 1 that we have conducted. We will come back to this issue in the next section.

4. The Steady State

Here we characterise the steady state by analytical predictions based on the model, compare these with the numerical results and show the dependence of the steady state on the two model parameters.

4.1. *Model-based Analytical Predictions*

We can find from the equations of the moments (3.6) that in the steady state, the Lagrangian and Eulerian mean of the supersaturation coincide $\langle S\rangle = \langle S\rangle_E$ as all time derivatives are zero and thus the mixed moments $\langle SR^x\rangle$ all vanish. The latter can only be fulfilled if the probability density function of the supersaturation s conditioned on any $R > 0$ is symmetric around zero. Due to the convergence of the mean droplet mass $\langle R^3\rangle$ and of the mean Eulerian supersaturation $\langle S\rangle_E$, the system (3.3) is no longer a stochastic integro-differential equation as it does not involve anymore integrals. Hence, it can be described by its associated stationary Fokker–Planck equation. To reflect the piecewise definition of the stochastic model (3.3), we split the joint probability density p into an atomic contribution m for evaporated droplets and a smooth part $\tilde{p}$ for active droplets

$$p\left(S, R^2, T\right) = m\left(S, T\right)\, \delta(R^2) + \tilde{p}\left(S, R^2, T\right)\,. \tag{4.1}$$

The stationary Fokker-Planck equation for the active droplets $\tilde{p}\left(S, R^2, T \to \infty\right)$ can then be written as

$$\frac{\partial}{\partial R^2}\left(S\tilde{p}\right) + \frac{\partial}{\partial S}\left(\left[\langle S\rangle_E - \left(1 + AR\right) S - \frac{\partial}{\partial S}\right]\tilde{p}\right) = 0\,. \tag{4.2}$$

Despite the simplifications in the steady state, finding a general solution is not straightforward because of the non-linear coupling term $(1 + AR)\, S$. Nevertheless, we can predict the shape of the tail of the distribution $p(R^2)$ of the droplet surface area. Interpreting the surface area R^2 as position and the supersaturation S as velocity, equation (4.2) is similar to the Fokker–Planck equation associated with Brownian particles subject to a position-dependent drag. In the large-drag limit the velocity is a fast variable and can be eliminated. Following Sancho *et al.* (1982), an expansion of the non-linear drag term yields to leading order

$$p(R^2) \simeq -\langle S\rangle_E \left(1 + AR\right) \exp\left(\langle S\rangle_E R^2 + \langle S\rangle_E \frac{2}{3} AR^3\right). \tag{4.3}$$

This solution is only valid when the term $(1 + AR)$ is dominant, *i.e.* for large droplets with $R^2 \gg 1/A^2$ (see Fig. 4). One could think of finding another solution for the opposite asymptotic $R^2 \ll 1/A^2$ and then match the two limiting solutions similarly to the approach in boundary layer theory. However, due to the finite probability of having completely evaporated droplets, see Eq. (4.1), and the complicated boundary conditions at $R = 0$, this is a very challenging task. Still, the large-droplet solution (4.3) has global consequences: To have an integrable distribution of large droplets the mean Eulerian supersaturation $\langle S \rangle_E$ has to be negative. As seen above, S conditioned on $R > 0$ has to be symmetric around zero, such that the mean value of S in the presence of droplets is zero. Hence, only S conditioned on $R = 0$ contributes to the negative $\langle S \rangle_E$. Therefore, it follows that the presence of completely evaporated droplets is a prerequisite for reaching the steady state.

4.2. *Comparison with Numerical Results*

In the following we show that the theoretical predictions for the PDFs of R^2 and S not only apply to the model but also to the DNS. In Fig. 6 the predictions, the MC simulations, and the DNS are contrasted by the means of the PDF of R^2 and the conditioned PDFs of S. For the case $C4$, which is presented in the upper half of Fig. 6, we know from Fig. 5 that the model predicts a slightly higher $\langle R^2 \rangle$ than the DNS. The PDF of R^2 obtained from the model shows a higher probability for intermediate-size droplets, which leads to this higher mean value. For $R^2 \gg 1/A^2$ the MC simulation fits the tail prediction (4.3). The tail of the PDF of the DNS is parallel to this prediction, *i.e.* the shapes match, up to a multiplicative constant. The PDF of the supersaturation S is shown conditioned on the droplet size. For evaporated droplets ($R^2 = 0$) the PDF of S has only negative values. For finite-size droplets the PDFs are centered at zero and nearly symmetric with practically constant variances, independent of the value of R^2 on which the PDF is conditioned. The model fits well the supersaturation PDFs of the DNS though some small deviations can be observed in the negative-S tail.

The trends discussed in the case $C4$ are representative for all DNS runs that we have conducted and are reported in Fig. 1. To corroborate this, we also show the data corresponding to the case $C6$ in the lower half of Fig. 6, which features smaller τ_c and τ_s, *i.e.* a larger A. The PDF of R^2 obtained with the model coincides with the prediction at large droplet sizes. Intermediate R's are less probable in the DNS but the shape of the tail fits. The PDFs of s are well reproduced. While the PDF of S for evaporated droplets looks very similar to that for the case $C4$, the active droplets damp the supersaturation more strongly due to the larger coupling parameter A. Because of a smaller variance of S the droplets are smaller in the case $C6$ than in the case $C4$.

4.3. *Characterisation By The Model Parameters*

In the steady state the system (3.3) depends only on the two model parameters, namely the coupling parameter A defined in (3.5) and the total mass $\langle W \rangle$ associated with the conservation of liquid and vapour (3.4). In Fig. 7 the steady state is characterised by the mean drop surface area, its relative standard deviation, and the mean Eulerian supersaturation which are represented as a function of A for various values of $\langle W \rangle$.

The mean drop surface area $\langle R^2 \rangle|_{R>0}$, displayed at the top of Fig. 7, shows approximately a power-law behaviour $\propto A^{-2/3}$. This can be explained by the conservation of mass (3.4). For large A the third moment of R corresponding to the mean drop mass has to decrease correspondingly. This argument also explains why $\langle R^2 \rangle|_{R>0}$ increases with $\langle W \rangle$. We would like to emphasize the fact that mean-field arguments predict no

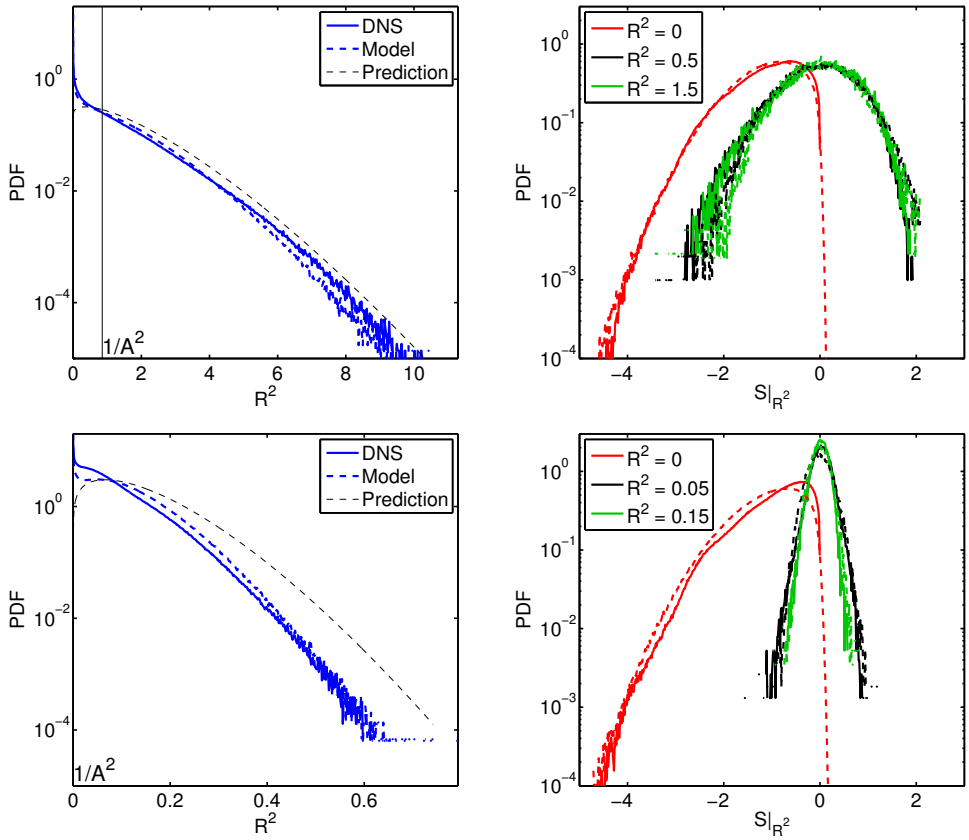

FIGURE 6. Left side: Probability density function of R^2 from the DNS (solid line) and the model (dashed line). The prediction from Eq. (4.3) is shown as thin dashed line. The value $1/A^2$ is indicated as a thin solid black line. Right side: Probability density function of S conditioned on three values of R^2. Again, the DNS results are drawn as solid lines while the results from the model are shown as dashed lines. The PDFs are computed for the case $C4$ (top row) and the case $C6$ (bottom row).

drop growth for an initially vanishing average supersaturation. In contrast, due to the supersaturation fluctuations $\langle R^2\rangle|_{R>0}$ always converges to a positive, non-zero value even for zero total mass in the system.

Following the same scaling arguments $\langle R^4\rangle$ is proportional to $A^{-4/3}$, such that, to leading order, $\sigma_{R^2}/\langle R^2\rangle|_{R>0}$ is expected to be constant. However, one finds in the middle of Fig. 7 that the size broadening slightly decreases with A. This can be explained by the tail prediction, since $\langle R^4\rangle$ depends strongly on the large droplets. For large A, the droplet size distribution has a sub-exponential tail given by (4.3). Consistently, the relative standard deviation features values smaller than 1, which decrease slowly with A. For A going to zero, an exponential distribution would be expected from Eq. (4.3), similarly to the case of Brownian motion with reflection. However, the shape prediction is only valid for $(1 + AR)$ large and hence the moments become dominated by the unknown small-drag distribution. The mean drop size increases with $\langle W\rangle$, so that the tail prediction is valid for a larger portion of the PDF of R^2 and $\sigma_{R^2}/\langle R^2\rangle$ becomes smaller.

A negative mean Eulerian supersaturation $\langle S\rangle_E$ is a requirement for a steady state

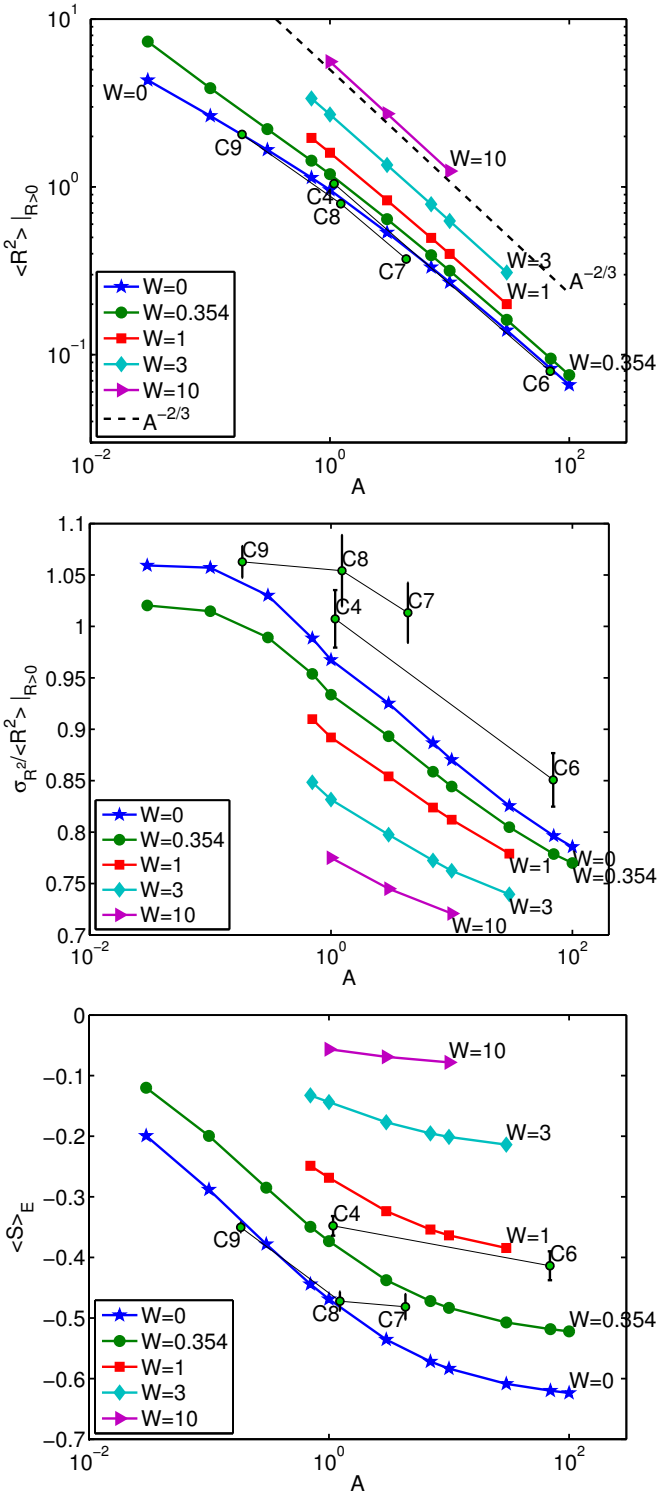

FIGURE 7. Steady-state values of the mean drop surface area $\langle R^2\rangle|_{R>0}$ (top), the relative standard deviation $\sigma_{R^2}/\langle R^2\rangle|_{R>0}$ (middle), and the mean Eulerian supersaturation $\langle S\rangle_E$ (bottom) as a function of A and with the water parameter $\langle W\rangle$ ranging from 0 to 10. For comparison with these model results the DNS values of the cases $C7$, $C8$, and $C9$ with $\langle W\rangle \sim 0$ and $C4$ and $C6$ with $\langle W\rangle \sim 0.354$ are superimposed.

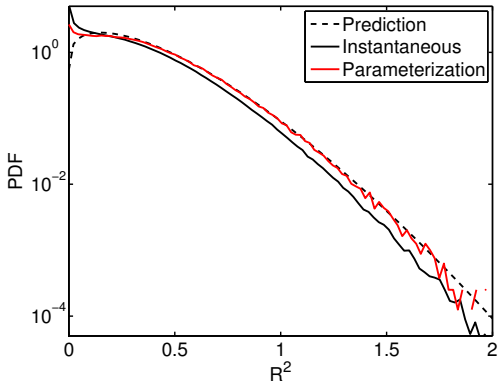

FIGURE 8. Comparison of the steady-state R^2 PDF of two MC simulations with different boundary conditions at $R = 0$. Black solid line: Instantaneous reactivation as soon as the supersaturation S is positive, according to Eq. (2.1); Red solid line: Activation according to a power-law parameterisation in S (Seifert & Beheng 2006); Black dashed line: Prediction given by Eq. (4.3).

(see §4.1). Note that

$$\langle S\rangle_E = \langle S\rangle = \langle S|R=0\rangle p\,(R=0) + \int \langle S|R\rangle p\,(R)\,dR = \langle S|R=0\rangle \times \frac{N_{evap}}{N}\,. \qquad (4.4)$$

Since the PDF of S conditioned on $R = 0$ seems to be independent of both A and $\langle W\rangle$ (see Fig. 6), the value of $\langle S\rangle_E$ is directly proportional to the number of evaporated drops. For a small coupling parameter A, the tendency for droplets to be pushed towards $R^2 = 0$ is low, so that most of them are active (see lower part of Fig. 7). As A increases, the steady-state fraction of evaporated droplets increases. This leads to more negative contributions to $\langle S\rangle_E$. The mean size $\langle R^2\rangle$ increases with $\langle W\rangle$, and therefore the distance to the zero-size boundary becomes larger. Hence, for larger $\langle W\rangle$, the probability for evaporated droplets is smaller and $\langle S\rangle_E$ is larger, closer to zero.

The DNS statistics are also shown in Fig. 7. These values are less certain, since, as visible in Fig. 5, they fluctuate more strongly and the fourth-order moment of R might not be fully converged to its steady-state value at the end of the simulation time of $20\,t_s$. As expected from Fig. 5, the DNS cases show lower mean values and higher relative standard deviations. Nevertheless, their scalings are consistent with the model results.

Finally, to show that the shape of the PDF of R^2 at large droplet sizes does not depend on the treatment of those with a size close to zero, the model is modified to activate droplets according to a parameterisation given by the Köhler-Kelvin theory (see, *e.g.*, Seifert & Beheng 2006). In this parameterisation the activation probability behaves as a power-law on S. Therefore the time a droplet spends at $R = 0$ until it is reactivated is increased. Hence, the number of evaporated drops in the steady state increases. However, as it can be seen in Fig. 8, the dynamics of large drops faraway from the boundary is practically unaffected. This is consistent with the findings of Celani *et al.* (2008) (see §1).

5. Transients

Depending on the physical situation, the time to reach the steady state can be too long compared to the time of interest such that the transient behaviour is of interest. As anticipated in the context of Fig. 5, the time evolution of the system (3.3) can be

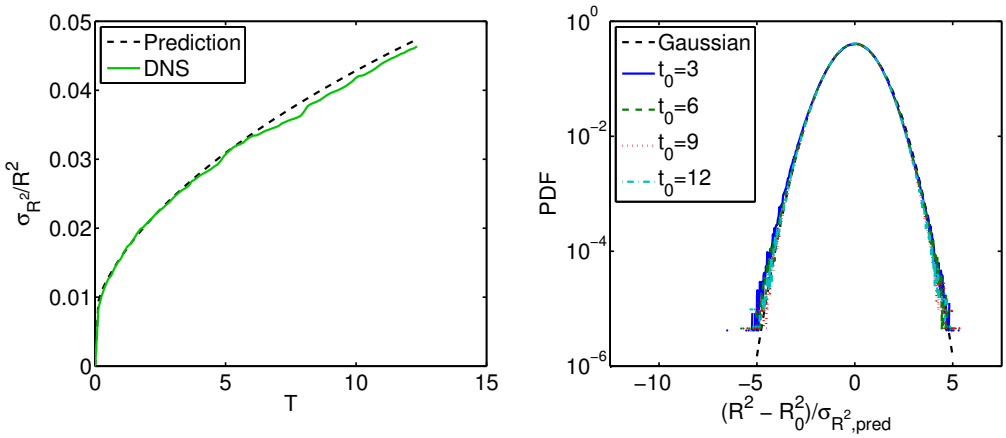

FIGURE 9. Short-time behaviour of the DNS in the case $C1$. Left: Relative standard deviation $\sigma_{R^2}/\langle R^2\rangle$ as a function of time (solid line), in comparison to the prediction of Eq. (5.1b) (dashed line). Right: PDF of R^2 standardized by the initial mean value $\bar{R}_0^2$ and the standard deviation $\sigma_{R^2,pred}$ predicted by Eq. (5.1b) at different times (solid lines) and in comparison with a standard Gaussian distribution (dashed line).

differentiated into two stages, a short-time and a long-time behaviour. In the following these two transients are described.

5.1. *Short-time Behaviour*

At short times the evolution of the system still depends on the initial conditions for S and R. We exemplarily explain the short-time behaviour of Eqs. (3.3) by concentrating on the DNS settings with a normally distributed supersaturation $S \sim \mathcal{N}(0,1)$, where $\mathcal{N}\left(\mu,\sigma^2\right)$ denotes a normal distribution with mean μ and a standard deviation σ and a monodisperse drop spectrum $\delta(R-R_0)$. Let us assume that, at short times, the mean droplet mass $\langle R^3\rangle$ and the coupling $(1+AR)$ remain approximately constant. The second assumption might seem a bit crude as we are interested in the evolution of the individual radii R. However, turbulent condensation models frequently assume that $\tau_s\bar{r}/r$ is constant, equal to $\langle\tau_s\rangle$, in order to obtain analytical solutions (see e.g. Sardina *et al.* 2015; Field *et al.* 2014). This can be justified globally, as the assumption of constant $\langle R^3\rangle$ implies $\langle SR\rangle = 0$, see Eq. (3.6a). Under such approximations the evolution of S greatly simplifies: Equation (3.3b) loses its dependence on an integral quantity ($\langle S\rangle_E \approx 0$), as well as its nonlinearity ($AR \approx$ const.). Hence, the dynamics of S are independent of R and follow a standard Ornstein–Uhlenbeck process, where R is just the time integration of this process. Therefore, the distributions of S and R are Gaussian and are fully determined by their first two moments. Using (3.6), the distributions of S and R^2 can be straightforwardly written as

$$S \sim \mathcal{N}\left(0\ ,\ \Theta + (1-\Theta)\exp\left(-2T/\Theta\right)\right) \tag{5.1a}$$

$$R^2 \sim \mathcal{N}\left(R_0^2, \Theta^2\left[2T + (4\Theta-2)\left(\exp\left(-T/\Theta\right)-1\right) + (1-\Theta)\left(\exp\left(-2T/\Theta\right)-1\right)\right]\right), \tag{5.1b}$$

with

$$\Theta = \frac{1}{1+AR} = \frac{1}{1+t_s/\tau_s} = \frac{1/t_s}{1/t_s+1/\tau_s} = \frac{\tau_s}{\tau_s+t_s} < 1, \tag{5.2}$$

where we have used the assumptions that $(1+AR)$ and $\langle\tau_s\rangle$ are constant.

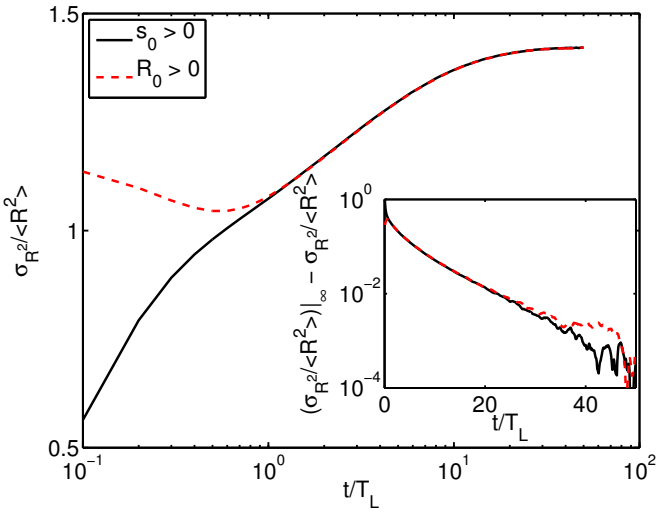

FIGURE 10. Time behaviour of the droplet surface normalized standard deviation $\sigma_{R^2}/\langle R^2\rangle$ in lin-log for two different initial conditions but the same model parameters A and $\langle W\rangle$. Red dashed line: Initially delta function in $R > 0$ and zero mean normal distribution for s; Black solid line: Initially zero sized droplets ($R = 0$) and constant positive $S > 0$. Inset: Same data but subtracted to the steady state value and in a log-lin plot.

These predictions are compared in Fig. 9 to the DNS results for the case $C1$. The initial time evolution of the relative standard deviation matches very well. This demonstrates that the droplets feel the supersaturation along their trajectory as if it was white noise because $\Theta \ll \tau_c/t_s$ (see §2.2). The resulting Brownian motion for the drop surface area leads to a Gaussian distribution with a variance increasing linearly with time. The time-dependent DNS distributions can be perfectly collapsed to a standard normal distribution using the predicted values. When time increases, the assumptions used to derive Eqs. (5.1) are violated, *e.g.*, $\langle R^3\rangle$ increases slightly with increasing σ_{R^2}. Nevertheless, the prediction for $\sigma_{R^2}/\langle R^2\rangle$ stays close to the DNS values.

The system behaviour changes drastically when the drop size distribution becomes so wide that some droplets start to completely evaporate. Thereby, they lose their memory of their past history and they thus become independent of their initial condition. This is apparent in Fig. 10 where the time evolutions of two MC simulations with different initial conditions but the same parameters A and $\langle W\rangle$ are compared. While the time evolutions depend on the initial conditions at short times and is thus very different, they converge towards each other and coincide at long times.

The time at which the diffusive short-time behaviour ends and a transition to the long-time behaviour starts is the time at which complete evaporation becomes significant. This evaporation time T_{evap} can be estimated as the time where $2\sigma_{R^2} \sim \langle R^2\rangle$. From (5.1$b$) one obtains (in the limit of $T \gg \Theta$)

$$\frac{t_{\text{evap}}}{t_s} \sim \frac{1}{8\Theta^2}\frac{\tau_c^2}{t_s^2} - \frac{1}{2} + \frac{3}{2}\Theta. \tag{5.3}$$

This time scale was already shown in Fig. 5 to mark the transition from the diffusive behaviour to the convergence to the steady state. If we want to observe the diffusive behaviour on timescales of the order of t_s, the time until first evaporation has to satisfy

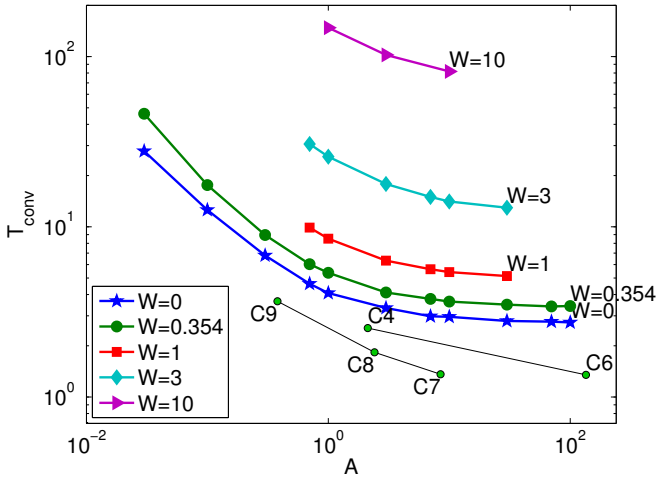

FIGURE 11. Exponential convergence time scale T_{conv} as a function of the parameter A and with the Scharparameter $\langle W \rangle$ ranging from 0 to 10. As in fig. 7 the DNS values of the cases $C7$, $C8$, and $C9$ with $\langle W \rangle \sim 0$ and $C4$ and $C6$ with $\langle W \rangle \sim 0.354$ are superimposed.

$t_{\text{evap}} > t_s$. For Θ small, this leads to

$$\tau_c > \frac{\sqrt{8}}{1/t_s + 1/\tau_s}. \tag{5.4}$$

Note that a harmonic mean of t_s and τ_s appears — see Eq. (5.2). This is very close to the initial phenomenological reasoning $\tau_c > \min(\tau_s, t_0)$ that was used to distinguish between the two regimes found in the DNS (see §2.2). Also Paoli & Shariff (2009) could collapse the time dependence of their DNS results by normalizing time with the harmonic mean of t_0 and τ_s. As rule of thumb it can be stated that the short-time behaviour containing no evaporated droplets is always present. However, when $\langle W \rangle$ is smaller than one, it is too short to be identified.

5.2. *Long-time Behaviour*

The long-time evolution of the system is independent of the initial conditions (see Fig. 10). It can be expected that the system converges exponentially fast to the steady state with a rate given by the largest eigenvalue of the Fokker-Planck equation associated with the stochastic dynamics (3.3). This is confirmed in the inset of Fig. 10. The exponential convergence time T_{conv} can be measured and is plotted in Fig. 11. The curves are very similar to the steady state values of $\langle s \rangle_E$ and the behaviour can be explained by the same arguments. The larger is the parameter A, the stronger is the bias due to the coupling term, *i.e.* the waiting time to be evaporated shortens. For large A the convergence time seems to saturate to approximately $2.75\, t_s$ for $\langle W \rangle = 0$. At larger masses $\langle W \rangle$, the convergence to the steady state is slower. Since the mean droplet size is larger (see Fig. 7), the time needed for droplets to completely evaporate increases. In DNS the convergence to the steady state is faster than in the model. This was already visible from Fig. 5, albeit it can also be seen that the measurements are less certain and the fluctuations of the moments of R are stronger. Nevertheless, the trends with respect to A and $\langle W \rangle$ seem to be consistent with the behaviour obtained from the model.

6. Summary and Concluding Remarks

We have shown in this study that under some rather broad assumptions, the problem of turbulent condensation depends on two parameters only and can be modeled and understood by a relatively simple stochastic system. The turbulent supersaturation fluctuations, together with the turbulent transport and mixing, offer different conditions for the growth of droplets. This can be modeled by a Lagrangian stochastic approach for the joint evolution of the squared droplet radius and the supersaturation along its trajectory. The two parameters are fixed by the total amount of water and the thermodynamic properties, as well as the Lagrangian integral timescale of the turbulent supersaturation. The model reproduces well the time evolution of droplet size distributions obtained from direct numerical simulations.

With the help of the model we can reconcile the results of the DNS studies in the literature by applying our findings to the other studies. Depending on the initial conditions and the considered time, different regimes in the evolution of the system can be found. For initially large drops, the time until the first evaporation is long (see Eq. (5.3)). Hence, first the supersaturation S converges on a timescale Θt_s from its initially droplet free variance $s^2_{\rm rms}$ to a smaller variance of size $\Theta s^2_{\rm rms}$ (see Eqs. (5.1)). This result can be found equal to the stochastic model prediction by Field *et al.* (2014) using the dimensional arguments of Lanotte *et al.* (2009) $s_{\rm rms} = a_1 u_{\rm rms} t_0$. Since it shares some similarities with the quasi-equilibrium supersaturation value in the case of no turbulence but constant supersaturation source (Grabowski & Wang 2013), it is called quasi-steady value in Lanotte *et al.* (2009) and Sardina *et al.* (2015). Hence, at times $t \gg \Theta$ the droplet surface area diffuses (§5.1). Sardina *et al.* (2015) obtained under the assumption $\tau_s \ll t_0$ an analytical expression for σ_{r^2} (their eq. 13) which reasonably matched their DNS results. Eq. (5.1) derived in §5.1 provides an identical dependence for σ_{r^2} if the difference between t_0 and t_s is ignored and $s_{\rm rms} = a_1 u_{\rm rms} t_0$ is used again. For smaller τ_c/t_0 complete evaporation occurs faster (Lanotte *et al.* 2009), so that $\langle s \rangle_E$ becomes negative (compare Celani *et al.* (2007)). Due to the associated memory loss the long-time behaviour characterised in §5.2 is observed (as for instance in Celani *et al.* 2005, 2008). Eventually, the steady state is reached (§4.1); the evolution of the droplet spectrum stops due to the fact that the average of s conditioned on $r > 0$ converges to zero (Celani *et al.* 2009). We found that in this statistical steady state, the droplet mass distribution exhibits an exponential tail. To conclude, we argue that the problem just features different regimes but is actually independent of the dimensionality, the kind of supersaturation forcing, the activation process, and so on, so that there is strong evidence that it is *universal*.

In this study we focused on homogeneous turbulent condensation. However, there is no obvious reason why the model (Eqs. 3.3) should not be applied to inhomogenous cases. For example the problem of mixing of sub- and supersaturated regions is based on the same governing equations. DNS show even similar trends for the PDF of r^2 (fig 3. of Kumar *et al.* 2012): The tail has a shape in between a Gaussian and an exponential. For problems with supersaturation sources and sinks such as temperature gradients, the mass $\langle W \rangle$ (Eq. 3.4) could be made dependent of position or time, respectively.

Nevertheless, high droplet volume loading or strong droplet inertia would certainly question the validity of the modeling. We have indeed assumed that the fluctuations of the supersaturation field along droplets follows a rather simple dynamics close to diffusion. However, it is known that particles with significant inertia tend to cluster in the fronts of an advected scalar (Wetchagarun & Riley 2010; Bec *et al.* 2014) leading to very intermittent Lagrangian statistics that cannot be reproduced by the model.

In the settings where droplet inertia can be neglected, such simple model can account for most of the effects of turbulence as the condensation/evaporation process is reversible and only one-drop one-time statistics are relevant. However, for the understanding of the spatial structure of the supersaturation field or the transition to a collision-induced growth, two-point statistics become important. Here, we expect non-trivial effects since turbulent transport can display anomalous scaling laws. By looking closely at Fig. 2 it can be seen that the droplet size and the local supersaturation value are correlated for newly activated, small droplets while this correlation vanishes for larger droplets whose size changes much slower. This means it is overproportionally likely to find equally sized, small droplets on isosurfaces of specific supersaturation values, *i.e.* it seems that a condensational clustering exists in absence of any droplet inertia.

We acknowledge H. Homann for very useful discussions. This research has received funding from the French Agence Nationale de la Recherche (Programme Blanc ANR-12-BS09-011-04). This work was performed using HPC resources from GENCI-TGCC (Grant 2015-2b6815) and from the Mesocenter SIGAMM hosted by the Observatoire de la Côte d'Azur.

Appendix A

In the manuscript vectorial quantities are set in bold, dimensional quanitities in lower case, and dimensionless quantities in upper case.

List of Symbols

A	coupling parameter
a_1	updraft forcing constant
a_2	supersaturation constant
a_3	condensation constant
l_0	large-scale lengthscale
N	number of droplets
N_x^3	number of spatial collocation points
n_d	droplet number density
p	pressure
Re	large-scale Reynolds number
R_λ	Taylor-scale based Reynolds numer
r	droplet radius
$\bar{r}$	characteristic, mass-averaged droplet radius
St	large scale Stokes number
Sc	Schmidt number
s	local supersaturation
$\langle s \rangle_E$	mean Eulerian supersaturation
s_{rms}	supersaturation standard deviation in absence of droplets
t	time
t_0	large-scale timescale
t_{conv}	convergence timescale
t_{evap}	time until first evaporation
t_u	integral timescale of the Lagrangian velocity autocorrelation
t_s	integral timescale of the Lagrangian supersaturation autocorrelation
$\mathbf{u}$	gasflow velocity
u_{rms}	root-mean-square velocity

$\mathbf{v}$	droplet velocity
$\langle W \rangle$	total mass parameter
w	total water mass
$\mathbf{x}$	position
ε	mean kinetic energy dissipation rate
ξ	standard white noise
η	Kolmogorov dissipative scale
Θ	time scale ratio
κ	molecular diffusivity of vapour inside the gas
ν	kinematic viscosity of the gasflow
ρ	density
σ	standard deviation
τ_c	condensation timescale
τ_d	droplet response time
τ_s	supersaturation timescale
τ_ν	viscous mixing time scale
τ_κ	diffusion mixing time scale
τ_η	Kolmogorov time
υ	volume
ϕ	forcing

REFERENCES

Bartlett, J.T. & Jonas, P.R. 1972 On the dispersion of the sizes of droplets growing by condensation in turbulent clouds. *Quart. J. Roy. Meteor. Soc* **98**, 150–164.

Bec, J., Homann, H. & Krstulovic, G. 2014 Clustering, fronts, and heat transfer in turbulent suspensions of heavy particles. *Phys. Rev. Lett.* **112**, 234503.

Celani, A., Falkovich, G., Mazzino, A. & Seminara, A. 2005 Droplet condensation in turbulent flows. *Europhys. Lett.* **70** (6), 775.

Celani, A., Lanotte, A., Mazzino, A. & Vergassola, M. 2001 Fronts in passive scalar turbulence. *Phys. Fluids* **13** (6), 1768–1783.

Celani, A., Mazzino, A., Seminara, A. & Tizzi, M. 2007 Droplet condensation in two-dimensional bolgiano turbulence. *J. Turbul.* **8**, N17.

Celani, A., Mazzino, A. & Tizzi, M. 2008 The equivalent size of cloud condensation nuclei. *New J. Phys.* **10** (7), 075021.

Celani, A., Mazzino, A. & Tizzi, M. 2009 Droplet feedback on vapor in a warm cloud. *Int. J. Mod Phys B* **23** (28n29), 5434–5443.

Devenish, B.J., Bartello, P., Brenguier, J.-L., Collins, L.R., Grabowski, W.W., IJzermans, R.H.A., Malinowski, S.P., Reeks, M.W., Vassilicos, J.-C., Wang, L.-P. & Warhaft, Z. 2012 Droplet growth in warm turbulent clouds. *Q. J. R. Meteorol. Soc.* pp. 1401–1429, DOI:10.1002/qj.1897.

Devenish, BJ, Furtado, K & Thomson, DJ 2016 Analytical solutions of the supersaturation equation for a warm cloud. *J. Atmos. Sci.* **73** (9), 3453–3465.

Field, PR, Hill, AA, Furtado, K & Korolev, A 2014 Mixed-phase clouds in a turbulent environment. part 2: Analytic treatment. *Q. J. R. Meteorol. Soc.* **140** (680), 870–880.

Gotoh, T. & Watanabe, T. 2015 Power and nonpower laws of passive scalar moments convected by isotropic turbulence. *Phys. Rev. Lett.* **115**, 114502.

Grabowski, W.W. & Wang, L.-P. 2013 Growth of cloud droplets in a turbulent environment. *Annu. Rev. Fluid Mech.* **45** (1), 293–324.

Homann, H., Dreher, J. & Grauer, R. 2007 Impact of the floating-point precision and interpolation scheme on the results of dns of turbulence by pseudo-spectral codes. *Comp. Phys. Comm.* **177** (7), 560–565.

Ingersoll, Andrew P, Dowling, Timothy E, Gierasch, Peter J, Orton, Glenn S,

Read, Peter L, Sánchez-Lavega, Agustin, Showman, Adam P, Simon-Miller, Amy A & Vasavada, Ashwin R 2004 Dynamics of jupiters atmosphere. In *Jupiter: The Planet, Satellites and Magnetosphere* (ed. F. Bagenal, T.E. Dowling & W.B. McKinnon), chap. 6. Cambridge Univ. Press.

Khvorostyanov, V.I. & Curry, J.A. 1999 Toward the theory of stochastic condensation in clouds. Part I: A general kinetic equation. *J. Atmos. Sci.* **56** (23), 3985–3996.

Kulmala, M., Rannik, Ü., Zapadinsky, E.L. & Clement, C.F. 1997 The effect of saturation fluctuations on droplet growth. *J. Atmos. Sci.* **28** (8), 1395–1409.

Kumar, B., Janetzko, F., Schumacher, J. & Shaw, R.A. 2012 Extreme responses of a coupled scalar–particle system during turbulent mixing. *New J. Phys.* **14** (11), 115020.

Lanotte, A.S., Seminara, A. & Toschi, F. 2009 Cloud droplet growth by condensation in homogeneous isotropic turbulence. *J. Atmos. Sci.* **66** (6), 1685–1697.

Lasher-Trapp, S.G., Cooper, W.A. & Blyth, A.M. 2005 Broadening of droplet size distributions from entrainment and mixing in a cumulus cloud. *Q. J. R. Meteorol. Soc.* **131** (605), 195–220.

Lehmann, K., Siebert, H. & Shaw, R.A. 2009 Homogeneous and inhomogeneous mixing in cumulus clouds: Dependence on local turbulence structure. *J. Atmos. Sci.* **66** (12), 3641–3659.

McGraw, R. & Liu, Y. 2006 Brownian drift-diffusion model for evolution of droplet size distributions in turbulent clouds. *Geophys. Res. Lett.* **33** (3).

Paoli, R. & Shariff, K. 2009 Turbulent condensation of droplets: Direct simulation and a stochastic model. *J. Atmos. Sci.* **66** (3), 723–740.

Pinsky, M, Mazin, IP, Korolev, A & Khain, A 2013 Supersaturation and diffusional droplet growth in liquid clouds. *J. Atmos. Sci.* **70** (9), 2778–2793.

Pope, S. B. 2000 *Turbulent flows*. Cambridge: Cambridge University Press.

Pruppacher, H. & Klett, J. 1997 *Microphysics of clouds and precipitation*. Kluwer Academic Publishers.

Reveillon, J. & Demoulin, F.-X. 2007 Effects of the preferential segregation of droplets on evaporation and turbulent mixing. *J. Fluid Mech.* **583**, 273–302.

Sancho, J.M., San Miguel, M. & Dürr, D. 1982 Adiabatic elimination for systems of brownian particles with nonconstant damping coefficients. *J. Stat. Phys.* **28** (2), 291–305.

Sardina, G., Picano, F., Brandt, L. & Caballero, R. 2015 Continuous growth of droplet size variance due to condensation in turbulent clouds. *Phys. Rev. Lett.* **115**, 184501.

Seifert, A & Beheng, KD 2006 A two-moment cloud microphysics parameterization for mixed-phase clouds. Part 1: Model description. *Meteorol. Atmos. Phys.* **92** (1-2), 45–66.

Shaw, R. A. 2003 Particle-turbulence interactions in atmospheric clouds. *Annu. Rev. Fluid Mech.* **35**, 183–227.

Sidin, R.S., IJzermans, R.H. & Reeks, M.W. 2009 A Lagrangian approach to droplet condensation in atmospheric clouds. *Phys. Fluids* **21** (10), 106603.

Squires, P 1952 The growth of cloud drops by condensation. I. General characteristics. *J. Sci. Res. A* **5** (1), 59–86.

Srivastava, R.C. 1989 Growth of cloud drops by condensation: A criticism of currently accepted theory and a new approach. *J. Atmos. Sci.* **46** (7), 869–887.

Twomey, S 1959 The nuclei of natural cloud formation part II: The supersaturation in natural clouds and the variation of cloud droplet concentration. *Geofisica pura e applicata* **43** (1), 243–249.

Vaillancourt, P.A., Yau, M.K., Bartello, P. & Grabowski, W.W. 2002 Microscopic approach to cloud droplet growth by condensation. Part II: Turbulence, clustering, and condensational growth. *J. Atmos. Sci.* **59** (24), 3421–3435.

Vaillancourt, P.A., Yau, M.K. & Grabowski, W.W. 2001 Microscopic approach to cloud droplet growth by condensation. Part I: Model description and results without turbulence. *J. Atmos. Sci.* **58** (14), 1945–1964.

Warhaft, Z 2000 Passive scalars in turbulent flows. *Annu. Rev. Fluid Mech.* **32** (1), 203–240.

Wetchagarun, S. & Riley, J.J. 2010 Dispersion and temperature statistics of inertial particles in isotropic turbulence. *Phys. Fluids* **22** (6), 063301.

Yeung, PK 2001 Lagrangian characteristics of turbulence and scalar transport in direct numerical simulations. *J. Fluid Mech.* **427**, 241–274.